Coherent photoproduction of the neutral-pion and η-meson on the deuteron at incident energies below 1.15 GeV

T. Ishikawa[1,*] A. Fix,[2] H. Fujimura,[1,†] H. Fukasawa,[1] R. Hashimoto,[1,‡] Q. He,[1,§] Y. Honda,[1] T. Iwata,[3] S. Kaida,[1]
J. Kasagi,[1] A. Kawano,[4] S. Kuwasaki,[1] K. Maeda,[5] S. Masumoto,[6] M. Miyabe,[1] F. Miyahara,[1,‖] K. Mochizuki,[1]
N. Muramatsu,[1] A. Nakamura,[1] K. Nawa,[1] Y. Obara,[6] S. Ogushi,[1] Y. Okada,[1] K. Okamura,[1] Y. Onodera,[1] K. Ozawa,[7]
Y. Sakamoto,[4] M. Sato,[1] H. Shimizu,[1] H. Sugai,[1,¶] K. Suzuki,[1,#] Y. Tajima,[8] S. Takahashi,[1] Y. Taniguchi,[1] Y. Tsuchikawa,[1,**]
H. Yamazaki,[1,††] R. Yamazaki,[1] and H. Y. Yoshida[8]

[1]*Research Center for Electron Photon Science (ELPH), Tohoku University, Sendai 982-0826, Japan*
[2]*Tomsk Polytechnic University, Tomsk 634050, Russia*
[3]*Department of Science, Faculty of Science, Yamagata University, Yamagata 990-8560, Japan*
[4]*Department of Information Science, Faculty of Liberal Arts, Tohoku Gakuin University, Sendai 981-3193, Japan*
[5]*Department of Physics, Graduate School of Science, Tohoku University, Sendai 980-8578, Japan*
[6]*Department of Physics, Graduate School of Science, University of Tokyo, Tokyo 113-0033, Japan*
[7]*Institute of Particle and Nuclear Studies (IPNS), High Energy Accelerator Research Organization (KEK), Tsukuba 305-0801, Japan*
[8]*Institute of Arts and Sciences, Yamagata University, Yamagata 990-8560, Japan*

Coherent photoproduction of the neutral-pion and η-meson on the deuteron, $\gamma d \rightarrow \pi^0 \eta d$, was experimentally studied at incident photon energies ranging from the reaction threshold to 1.15 GeV. The total cross section demonstrates a rapid rise below 1 GeV. The data are underestimated by the existing theoretical calculations based on quasifree $\pi^0 \eta$ photoproduction on the nucleon followed by deuteron coalescence. At the same time, the data are rather well reproduced by the calculations taking into account the final-state interaction. We also measured for the first time the differential cross sections: the $\pi^0 \eta$ invariant-mass distribution $d\sigma/dM_{\pi\eta}$, the $\pi^0 d$ invariant-mass distribution $d\sigma/dM_{\pi d}$, the ηd invariant-mass distribution $d\sigma/dM_{\eta d}$, and the distribution over the deuteron emission angle $d\sigma/d\Omega_d$ in the overall center-of-mass frame. The measured cross section $d\sigma/d\Omega_d$ does not exhibit strongly backward-peaking behavior predicted by the calculations. At all incident energies, an increase in $d\sigma/dM_{\eta d}$ near the ηd threshold is observed, which indicates a bound or virtual ηd state resulting from a strong attraction between η and a deuteron. The possibilities of using coherent $\pi^0 \eta$ photoproduction on a nucleus to study the η-nuclear interaction are also discussed.

I. INTRODUCTION

Meson-nucleus interactions provide crucial insight into quantum chromodynamics (QCD) as a fundamental theory of strong interaction in the nonperturbative regime, where a meson is considered an excitation of the QCD vacuum described by various nonvanishing condensates. The properties of a meson may change in a nucleus due to the partial restoration of chiral symmetry, leading to a decrease of the chiral condensate [1–3]. Among mesons, the η meson (η) is one of the interesting particles because of η-η' mixing [4–6] and coupling with a nucleon (N) to the nucleon resonance $N(1535)1/2^-$, which is a candidate for the chiral partner of N [7–14]. A traditional tool for studying the η-nuclear interaction is the single η production from a nucleus. A significant increase in the η yield at low relative η-nuclear momenta observed in the reactions $pd \rightarrow \eta\,{}^3\mathrm{He}$ [15], $dp \rightarrow \eta\,{}^3\mathrm{He}$ [16,17], $\gamma\,{}^3\mathrm{He} \rightarrow \eta\,{}^3\mathrm{He}$ [18–20], and $\gamma\,{}^7\mathrm{Li} \rightarrow \eta\,{}^7\mathrm{Li}$ [21,22] may be interpreted as a signature of attractive forces between η and the nucleus.

A significant amount of information on the low-energy η-nuclear dynamics has been obtained from the final-state interactions (FSIs) in the reactions $pn \rightarrow \eta d$ [23,24] and $pd \rightarrow$

ηpd [25,26]. Despite large cross sections of these hadronic processes, their analysis can be complicated by various ambiguities associated with the initial-state interaction as well as with dominance of various two-step mechanisms, leading to undesirable model dependence [27].

These disadvantages can be overcome by turning to electromagnetic processes. At first, the electromagnetic interaction may be included perturbatively up to the first order in α_{em}, so that it is not necessary to take into account the initial-state interaction. The coherent photoproduction of $\pi^0\eta$ pairs on a nucleus, $\gamma A \to \pi^0\eta A$, considered in detail in Ref. [28] is especially suitable for studying the η-nuclear interaction under controlled conditions. Although there are three hadrons in the final state of such reactions, the π^0-nuclear interaction is expected to result in a trivial decrease of the π^0 yield due to absorption by the residual nucleus. This effect is well described on a phenomenological level, and it is thus well under control. In addition, the $\pi^0\eta$ interaction is small at least at low energies below $a_0(980)$ [29]. Furthermore, in these reactions, the major fraction of the transferred momentum is carried away by π^0 because of its small mass. As a result, an essential part of the available kinematic region corresponds to the low relative momentum between η and the nucleus, i.e., events in which the interaction between these particles is of particular importance.

An additional advantage of $\gamma A \to \pi^0\eta A$ is that the underlying elementary process $\gamma N \to \pi^0\eta N$ is rather well understood. According to various studies [21,30–47], the dominant mechanism of $\pi^0\eta$ photoproduction is the excitation of the $\Delta(1700)3/2^-$ and $\Delta(1940)3/2^-$ resonances, followed by their decay into the $\eta\Delta(1232)3/2^+$, and successively into the final $\pi^0\eta N$ state. The dominance of the isospin $I = 3/2$ part leads to an approximate equality of the elementary amplitudes on the proton and neutron, being in good agreement with the experimental data [45]. Due to the isoscalar nature of the deuteron, the proton and the neutron amplitudes are added coherently in $\gamma d \to \pi^0\eta d$. This relatively simple picture distinguishes $\gamma d \to \pi^0\eta d$ from the hadronic processes such as $pd \to \eta pd$, where the main reaction mechanism is still not very well understood.

In this paper, we study the $\gamma d \to \pi^0\eta d$ reaction, in order to better understand the mechanism for coherent $\pi^0\eta$ photoproduction on a nucleus. We have substantially extended our study from Ref. [48] and systematically analyzed the measured distributions, including additional ones, by comparing them with theoretical calculations. The organization of the paper is as follows. Our photoproduction experiment using a detector based on electromagnetic calorimeters is described in Sec. II. The analysis for selecting the $\gamma d \to \pi^0\eta d$ events is discussed in Sec. III. In Sec. IV, presented are the results for the total and differential cross sections. We determine the low-energy ηd scattering parameters from the phenomenological analysis of the results in Sec. V. Finally, we summarize our results in Sec. VI.

II. EXPERIMENT

A series of meson production experiments [49] were conducted using a bremsstrahlung-photon beam [50] from a primary 1.20-GeV electron beam in a synchrotron called the STretcher Booster (STB) ring [51] at the Research Center for Electron Photon Science (ELPH) [52], Tohoku University, Japan. The photon beam was provided by inserting a carbon fiber (radiator) [53] into the stored electrons in the STB ring, and then collimated with two lead apertures of 10 and 25 mm diameter located at 4.2 and 12.9 m downstream from the radiator, respectively. A cycle of providing a photon beam in the range from 12 to 26 s involved the following stages: (1) injection of 0.15-GeV electrons from a linear accelerator, (2) acceleration of the electrons up to 1.20 GeV, (3) production of bremsstrahlung photons by the radiator, and (4) preparation for the next cycle. In the third stage, the radiator gradually moved towards the center of the circulating electrons so as to produce a constant-intensity photon beam. The durations of this stage were different (6–20 s) for different experimental periods. The typical photon intensity was 360 MHz at normal operation (for the shortest cycle).

To monitor the position and size of the photon beam, the two-dimensional intensity map at the target location was regularly measured [50,54]. The photon-beam size was $\approx$6.5 and $\approx$7.5 mm in the standard deviation for the x (horizontal) and y (vertical) directions, respectively. The photon energy was determined by detecting the post-bremsstrahlung electron with a photon-tagging counter, STB-Tagger II [50]. The typical photon-tagging rate was 20 MHz, corresponding to the photon intensity of 360 MHz, and the tagging energy of the photon beam ranged from 0.75 to 1.15 GeV. The tagging signal did not always correspond to a photon arrival at the target since the electron from Møller scattering or Coulomb multiple scattering at the radiator may come to the tagging counter, or the photon may disappear by converting into a positron-and-electron pair even if the corresponding post-bremsstrahlung electron was correctly detected. Moreover, the electrons entering the tagging counter may be electrons produced by scattering or reaction with the residual gas in the STB ring. Thus, the photon transmittance (so-called tagging efficiency), which is the probability for the photon to reach the target when the electron is detected by the tagging detector, was also regularly measured [50,55]. The average of the photon transmittance was $\approx$53% (different for different photon-tagging channels [50], and almost constant for different experimental periods in each channel).

The target used in the present experiment was liquid deuterium stored in a cryostat, which consisted of a refrigerator, a heat transfer pipe including a target cell, and a heat shield. The refrigerator was a two-stage Gifford-McMahon (GM) cryocooler (Sumitomo Heavy Industries RKD-415D). It was vertically mounted at 920 mm upstream of the target center and attached to the heat transfer pipe leading to the target center because the target was surrounded with detector modules except for the beam hole. The pipe was made of 99.99% pure aluminum to obtain high thermal conductivity. The length of the pipe was 1000 mm and the cell was located at its end. The thickness of the cell was 40 mm, and the inner and outer diameters measured 61 and 65 mm, respectively. The cell was separated from vacuum with the entrance and exit windows made of aramid foil with a thickness of 12.5 μm. Since each window was thin and deformed when liquid deuterium was
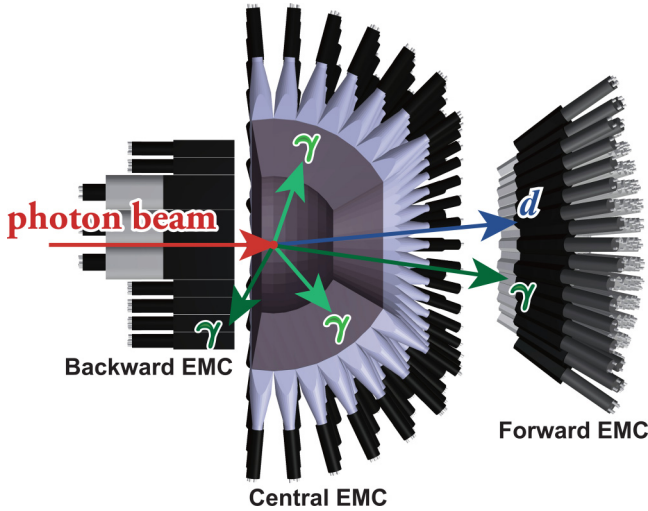
FIG. 1. Cross-section view of FOREST. It consists of three electromagnetic calorimeters (EMCs): the forward EMC consists of 192 pure CsI crystals, the central is comprised of 252 lead scintillating-fiber sandwich modules, and the backward has 62 Cherenkov counters made up of lead glass. The energy resolution of each EMC is approximately 3% (forward), 7% (central), and 5% (backward) for 1-GeV photons. A plastic-scintillator hodoscope (omitted in the figure) is placed in front of each EMC to identify charged particles.

filled into the cell, the displacements of the window at several positions were measured with a laser displacement meter (KEYENCE LK-H155) by means of a laser triangulation method [56]. The effective thickness of the deuterium target was found to be 45.9 mm from the measured displacements and the intensity map of the photon beam. Details of the liquid deuterium target can be found elsewhere [57,58].

All the final-state particles in the $\gamma d \rightarrow \pi^0 \eta d$ reaction were measured with the FOREST detector [58] depicted in Fig. 1. FOREST consisted of three different electromagnetic calorimeters (EMCs): 192 pure cesium iodide (CsI) crystals for the forward EMC, 252 lead scintillating-fiber sandwich modules for the central, and 62 lead-glass Cherenkov counters for the backward. The energy responses of the prototype EMCs were investigated using 100–800 MeV positron beams for testing detectors at ELPH [59], and the energy resolutions were found to be approximately 3%, 7%, and 5% in response to 1-GeV photons for the forward, central, and backward EMCs, respectively [58]. A plastic-scintillator hodoscope (PSH) was placed in front of each EMC to identify charged particles. The forward PSH consisted of left- and right-handed spiral-shaped plastic scintillators, and it could determine the impact position of a charged particle even when no corresponding EMC module was found. FOREST covered the solid angle of 88% in total.

The digitized data of the energies and timings for signals from STB-Tagger II and FOREST were acquired with a network-based data acquisition (DAQ) system developed for the FOREST experiments [58,60]. The DAQ system consisted of five collector subsystems, an event-builder subsystem, and a recorder subsystem. The collector subsystem read out the digitized data from the front-end electronics in parallel with

the other collector subsystems and converted the data into a single data fragment. The event builder gathered the fragments from all the collectors and constructed a physics event. The recorder stored the events in a hard disk. The trigger condition of the DAQ system for processing an event was made for detecting more than one particle in coincidence with a photon-tagging signal [58], and was the same as that in Refs. [61–63]. The trigger rate was 1.7 kHz on average, and the DAQ efficiency was 79% on average [62]. The details of the DAQ system can be found elsewhere [60].

Regarding the deuterium target at the circulating electron energy of 1.20 GeV, the number of the events acquired was 2.3×10^9 in total, and that of the corresponding tagging signals was 2.0×10^{13}. Additionally, we took 2.1×10^9 and 2.4×10^8 events, corresponding to 3.1×10^{13} and 9.7×10^{12} tagging signals, for the hydrogen and empty targets at the same electron energy, respectively. The data acquired with the hydrogen target were mainly used for checking consistency of geometries, resolutions, and efficiencies of the detector elements in FOREST. Those with the empty target were used to confirm that the nontarget contributions, mainly from the two sheets of 12.5-μm-thick aramid foil, are negligibly small. The details of the collected data can be found elsewhere [64].

III. EVENT SELECTION

When a photon entered a module in an EMC, not only this module but also the neighboring modules had a finite energy generated by the electromagnetic (EM) shower. To obtain the energy and incident position of the photon, we grouped a set of modules as an EMC cluster to which the particles in an EM shower deposited energies. The energy of the EMC cluster was basically given by the sum of the energies of the cluster members. A minor correction was made to take into account the energy leakage from the EMC modules. The incident position was reconstructed by a rational function using the energies of the maximum-energy module and the adjacent modules. This position-reconstruction method was studied using the data obtained in the beam tests for the prototype EMCs where positrons were perpendicularly incident on the front face of a module. Thus the position of the cluster, determined as an average of the front-face centers of modules in the cluster with energy-dependent weights, was slightly shifted from the actual incident position due to the finite injection angle for the forward and backward EMCs. It should be noted that the front face of each module in the central EMC is orthogonal to the line extending from the target center. The corrections due to the mentioned shift were determined by considering the depth at the maximum energy deposit of the EM shower. The energy calibration of each EMC module was performed in such a way that the π^0 peak in the $\gamma\gamma$ invariant-mass distribution corresponds to the π^0 mass. Details of the energy and position reconstruction, including energy calibration, are described in Ref. [58].

The event selection was carried out for the $\gamma d \rightarrow \pi^0 \eta d \rightarrow \gamma\gamma\gamma\gamma d$ reaction. Initially, events containing four neutral particles and a charged particle were selected. The EMC cluster without the corresponding PSH hit was recognized as a neutral particle. The PSH hit gave a charged

particle regardless of the presence of the corresponding EMC cluster. The time difference between any two of the four neutral EMC clusters was required to be less than three times the time resolution depending on the EMCs that the two clusters belonged to and the energies they deposited. The events were selected in such a way that a charged particle was detected with the forward PSH provided that the time delay from the response of the four neutral clusters was greater than 1 ns, and the deposit energy of a charged particle in PSH was larger than twice that of the minimum-ionizing particle.

Further selection was made by applying a kinematic fit (KF) with six constraints (6C) for the $\gamma d \rightarrow \pi^0 \eta d$ hypothesis (CKF): the energy and the three-momentum are conserved between the initial and final states, the invariant mass of two of the four photons is equal to the π^0 mass, and that of the other two photons is equal to the η mass. In each event, the most probable combination of dividing the four photons into two groups of two photons, each group corresponding to the π^0 and η mesons, was chosen. The momentum of the charged particle was obtained from the time delay under the assumption that the charged particle has the deuteron mass. Only those events were selected whose χ^2 probability (probability value for resulting χ^2 with the degrees of freedom in a fit) was greater than 0.2 in order to reduce the number of events from other background reactions. The most competitive background contribution came from deuteron misidentification in the quasifree (QF) reaction $\gamma p' \rightarrow \pi^0 \eta p$, where p' denotes the proton bound in the deuteron. Thus, an additional criterion for the selected events was the requirement that the χ^2 probability is less than 0.01 in another KF for the $\gamma p' \rightarrow \pi^0 \eta p$ hypothesis (QFKF). In this QFKF, the x, y, and z momenta of the initial bound proton were assumed to be measured with a centroid of 0 MeV/c and a resolution of 40 MeV/c, and its total energy was obtained assuming that the spectator neutron is always on shell. Finally, sideband-background subtraction was performed for accidental-coincidence events detected in STB-Tagger II and FOREST.

The 6C KF was rather effective for selecting the $\gamma d \rightarrow \pi^0 \eta d$ reaction. Figure 2 shows the correlation between the energy measured with PSH and the momentum of a charged particle in the coherent $\gamma d \rightarrow \pi^0 \eta d$ reaction and in the QF $\gamma p' \rightarrow \pi^0 \eta p$ reaction. Here, the momentum of the charged particle is determined as the difference between the incident-photon momentum and four final-state photon momenta:

$$\vec{p}_X = \vec{p}_0 - \sum_{i=1}^{4} \vec{p}_i, \qquad (1)$$

where $\vec{p}_0$ stands for the momentum of the incident photon, and $\vec{p}_i (i = 1, \ldots, 4)$ denotes that of the ith final-state photon from the π^0 or η decays. Since the momentum of the target deuteron is zero, $\vec{p}_X$ equals the momentum of the final-state deuteron. In Fig. 2, the events for each reaction were selected by the only requirement that the χ^2 probability is larger than 0.2 in the corresponding KF. Here, the additional requirement (χ^2 probability is lower than 0.01 in QFKF) was not applied for selecting the coherent events. The deuteron-detected events were correctly selected in CKF, and the proton-detected events were selected in QFKF. Background contamination
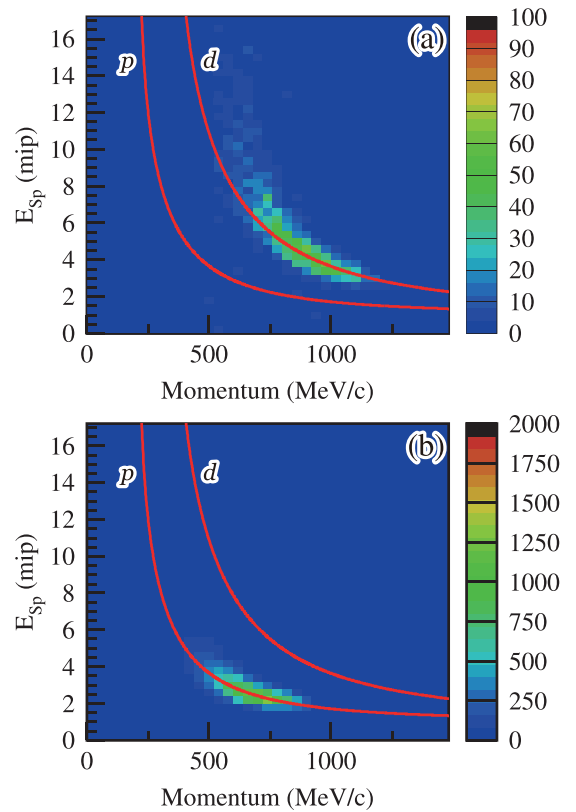

FIG. 2. Correlations between the measured energy with PSH and momentum of a charged particle in the (a) coherent $\gamma d \rightarrow \pi^0 \eta d$ reaction and (b) QF $\gamma p' \rightarrow \pi^0 \eta p$ reaction. Here the absolute value of the missing momentum $\vec{p}_X$ is provided for the $\gamma d \rightarrow \pi^0 \eta X$ reaction. The lower and upper curves in each panel show the loci corresponding to correlations for protons (p) and deuterons (d), respectively.

was taken into account in the event selection described above using CKF (χ^2 probability was higher than 0.2) and QFKF (χ^2 probability was lower than 0.01). Figure 3 shows the experimentally obtained χ^2 probability distribution in CKF for $E_\gamma = 1.01$–1.15 GeV together with those for the coherent $\gamma d \rightarrow \pi^0 \eta d$ reaction and the possible background reactions. The QF $\gamma p' \rightarrow \pi^0 \eta p$ reaction (QFp) was the most competitive among the background reactions, having ten times larger total cross section at maximum [44]. The χ^2 probability distribution in CKF was estimated for QFp when the χ^2 probability was less than 0.01 in QFKF. To incorporate the acceptance of the events in the FOREST detector, we adopted a Monte Carlo (MC) simulation code based on GEANT4 [65–67]. In this QFp simulation, the Fermi momentum of the initial bound proton was determined using the Hulthén wave function [68] with parameters $(\alpha, \beta) = (45.6, 234)$ MeV which reproduce the momentum distribution of nucleons in a deuteron derived from the $d(e, e'p)n$ reaction [69]. The total energy of the initial proton was evaluated in the same way as in QFKF. The three-momenta of the final-state particles were obtained by the pure phase-space generation at the center-of-mass (c.m.) energy of the incident photon and initial bound proton $W_{\gamma p'}$. The lower limit 0.2 in CKF made the QFp contamination less than 0.5%.
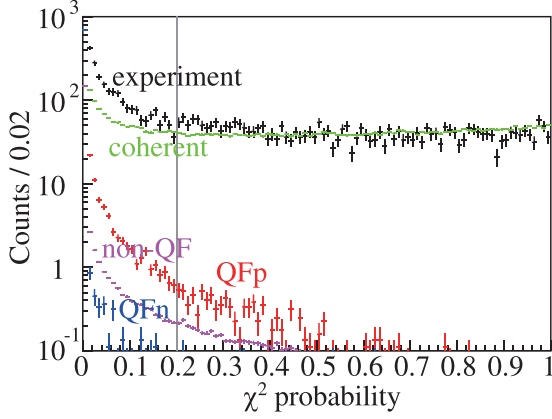
FIG. 3. χ^2 probability distributions in CKF for the experimental data, the coherent $\gamma d \to \pi^0 \eta d$ reaction, and the possible background reactions. The distributions are plotted for the highest-energy group of photon-tagging channels divided into four ($E_\gamma = 1.01$–1.15 GeV). The χ^2 probability is lower than 0.01 in QFKF. The black markers show the distribution for the experimental data, and the green, red, blue, and magenta represent the distributions for the coherent, QFp, QFn, and non-QF reactions, respectively.

The QF $\gamma n' \to \pi^0 \eta n$ reaction (QFn) was also considered as a candidate for the background reactions since the charged particle could be emitted when the neutron was passing through the material. The χ^2 probability distribution for QFn was estimated similarly to that for QFp. The QFn contamination was found to be much less than 0.1%. The non-quasi-free $\gamma d \to \pi^0 \pi^0 pn$ reaction (non-QF) could be a possible background although the total cross section for non-QF was negligibly small [44]. The χ^2 probability distribution was estimated for non-QF assuming the pure phase-space generation. The non-QF contamination was found to be less than 0.2% even if the total cross section is one-tenth of the coherent reaction as shown in Fig. 3.

IV. CROSS SECTIONS

Here, we deduce the cross sections for $\gamma d \to \pi^0 \eta d$. In Sec. IV A, we describe the method used to estimate the acceptance for this reaction. The total, differential, and double-differential cross sections are presented in Secs. IV B, IV C, and IV D, respectively.

A. Acceptance

The acceptance of $\gamma\gamma\gamma\gamma d$ detection for the $\gamma d \to \pi^0 \eta d$ events depends on the kinematic condition determined by detector efficiencies, geometrical acceptance, and event selection in the analysis. Thus, acceptance was estimated by the MC simulation code as a function of the kinematic binning for the cross section. The generated events in the simulation were reconstructed with the same analysis code which had been used for the experimental data. The acceptance for a given incident energy E_γ and kinematic condition $\mathcal{K}$, specified by a set of momentum vectors for all the final-state particles, is

given by

$$\mathcal{A}(E_\gamma, \mathcal{K}) = \frac{\mathcal{N}_{\mathrm{acc}}(E_\gamma, \mathcal{K})}{\mathcal{N}_{\mathrm{gen}}(E_\gamma, \mathcal{K})}, \qquad (2)$$

where $\mathcal{N}_{\mathrm{gen}}(E_\gamma, \mathcal{K})$ and $\mathcal{N}_{\mathrm{acc}}(E_\gamma, \mathcal{K})$ denote the number of the generated events and that of accepted events for $\mathcal{K}$, respectively. Since the $\gamma d \to \pi^0 \eta d$ reaction has three particles in the final state, the number of independent variables is five to specify $\mathcal{K}$, and it is reduced to four assuming rotational invariance with respect to the photon beam axis. Also assumed is an additional rotational symmetry of the plane spanned by the momenta of two final particles in the overall c.m. frame with respect to the momentum of the third particle. In this regard, we have chosen the following three variables for fixing $\mathcal{K}$: the $\pi^0 d$-invariant mass $M_{\pi d}$, the ηd-invariant mass $M_{\eta d}$, and the deuteron emission angle θ_d in the overall c.m. frame with the z axis along the incident photon momentum (the azimuth ϕ_d drops out due to the rotational symmetry mentioned above).

To determine the total cross section, we have to obtain the expected value of $\mathcal{A}(E_\gamma, \mathcal{K})$ for all possible $\mathcal{K}$s:

$$\mathcal{A}(E_\gamma) = \langle \mathcal{A}(E_\gamma, \mathcal{K}) \rangle = \frac{\sum_{\mathcal{K}} \mathcal{N}_{\mathrm{acc}}(E_\gamma, \mathcal{K})}{\sum_{\mathcal{K}} \mathcal{N}_{\mathrm{gen}}(E_\gamma, \mathcal{K})}. \qquad (3)$$

Similarly, we have to obtain the expected value at a fixed V_i to deduce the differential cross section as a function of V_i:

$$\mathcal{A}(E_\gamma, V_i) = \langle \mathcal{A}(E_\gamma, \mathcal{K}[V_i]) \rangle = \frac{\sum_{\mathcal{K}[V_i]} \mathcal{N}_{\mathrm{acc}}(E_\gamma, \mathcal{K})}{\sum_{\mathcal{K}[V_i]} \mathcal{N}_{\mathrm{gen}}(E_\gamma, \mathcal{K})}, \qquad (4)$$

where it is explicitly denoted that $\mathcal{K}$ depends on the running variable V_i. It should be emphasized that V_i does not have to be one of the kinematic variables $M_{\pi d}$, $M_{\eta d}$, or $\cos \theta_d$. Apparently, $\mathcal{A}(E_\gamma)$ and $\mathcal{A}(E_\gamma, V_i)$ depend on $\mathcal{N}_{\mathrm{gen}}(E_\gamma, \mathcal{K})$. Thus, the event generation should be adjusted to reproduce the measured distributions over $M_{\pi d}$, $M_{\eta d}$, and $\cos \theta_d$.

Because of the limited statistics, each distribution for the accepted events was compared to the measured one for each of three higher-energy groups of photon-tagging channels divided into the three bins ($E_\gamma = 0.85$–0.94, 0.95–1.01, 1.01–1.15 GeV). For comparison, histograms with a bin width of 10 MeV for the $M_{\pi d}$ and $M_{\eta d}$ distributions, as well as histograms with a bin width of 0.2 for $\cos \theta_d$, were built. The pure phase-space event generation has been changed to reproduce all the measured $M_{\pi d}$, $M_{\eta d}$, and $\cos \theta_d$ distributions within the statistical uncertainties. Here, a factorized weight was introduced for providing $\mathcal{N}_{\mathrm{gen}}(E_\gamma, \mathcal{K})$ with continuous and smooth functions: $w_{\pi d}(E_\gamma, M_{\pi d})$, $w_{\eta d}(E_\gamma, M_{\eta d})$, and $w_d(E_\gamma, \cos \theta_d)$.

B. Total cross section

The total cross section of the $\gamma d \to \pi^0 \eta d$ reaction was obtained according to the formula

$$\sigma(E_\gamma) = \frac{\mathcal{N}_{\pi\eta d}(E_\gamma)}{\mathcal{N}'_\gamma \mathcal{N}_\tau \mathcal{A}(E_\gamma) \mathcal{B}(\pi^0 \to \gamma\gamma) \mathcal{B}(\eta \to \gamma\gamma)}, \qquad (5)$$

containing the number of events for the $\gamma d \to \pi^0 \eta d$ reaction, $\mathcal{N}_{\pi\eta d}(E_\gamma)$, the effective number of incident photons, $\mathcal{N}'_\gamma$, the number of target deuterons per unit area, $\mathcal{N}_\tau = 0.237$ b^{-1}
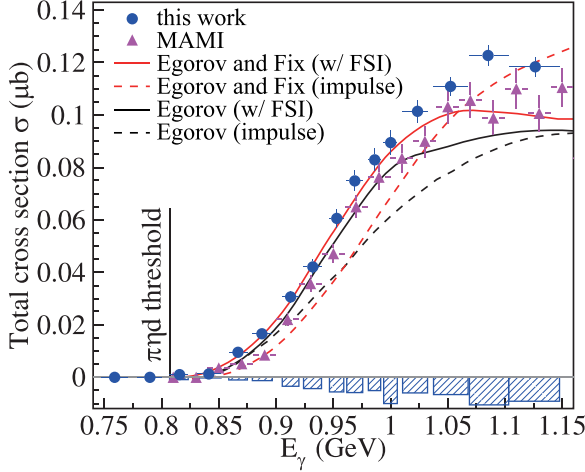
FIG. 4. Total cross section σ as a function of the incident photon energy E_γ. The blue circles show σ obtained in this work, and the magenta squares show that obtained at the MAMI facility [44]. The horizontal error of each data point corresponds to the coverage of the incident photon energy, and the vertical error shows the statistical error of σ. The lower hatched histogram shows the systematic error of σ in this work. The data are compared with the theoretical calculations given by Egorov and Fix [28] (red curves) and by Egorov [71] (black curves). The dashed and solid curves are obtained with the impulse approximation and with FSI, respectively.

corresponding to the thickness of 45.9 mm, the acceptance of the final state $\pi^0 \eta d \to \gamma\gamma\gamma\gamma d$ detection, $\mathcal{A}(E_\gamma)$, and the branching ratio of the $\pi^0 \to \gamma\gamma$ decay, $\mathcal{B}(\pi^0 \to \gamma\gamma) = 98.823\%$, and that of the $\eta \to \gamma\gamma$ decay, $\mathcal{B}(\eta \to \gamma\gamma) = 39.41\%$ [70]. $\sigma(E_\gamma)$ was obtained for each group of photon-tagging channels divided into 16 intervals. The number of incident photons, $\mathcal{N}_\gamma$, was determined by multiplying the number of tagging signals after the counting-loss correction by the corresponding photon transmittance. $\mathcal{N}'_\gamma$ was additionally obtained by multiplying $\mathcal{N}_\gamma$ by the DAQ efficiency. Figure 4 shows the total cross section σ as a function of the incident photon energy E_γ.

We estimated the following systematic uncertainties pertaining to the σ measurement: yield extraction associated with event selection in KF; acceptance correction arising from the $M_{\pi d}$, $M_{\eta d}$, and $\cos\theta_d$ distributions in event generation of the simulation, from the FOREST coverage, and from the detection efficiency of deuterons; and normalization resulting from the numbers of target deuterons and incident photons. At first, to obtain the systematic uncertainty in KF, we changed the lower limit of event selection in CKF from 0.1 to 0.5. We considered the standard deviation of the numbers of the accepted events, ranging from 4% to 6%, as the uncertainty. Since all relative uncertainties, except that for the overall normalization, became larger with decreasing the incident photon energy, we have taken here those for the incident photon energy higher than 1 GeV as typical values. To obtain the effects of the uncertainties of the assumed distributions in event generation, we introduced an additional factor:

$$w_i(E_\gamma, R_i) = 1 + \alpha_i R_i(E_\gamma, V_i), \tag{6}$$

where V_i is a variable from the set $M_{\pi d}$, $M_{\eta d}$, and $\cos\theta_d$. R_i is a real value obtained from V_i by mapping to the interval [0,1]:

$$R_i(E_\gamma, V_i) = \frac{V_i - V_i^{\min}(E_\gamma)}{V_i^{\max}(E_\gamma) - V_i^{\min}(E_\gamma)}. \tag{7}$$

The variation of the estimated acceptance was taken as an uncertainty when α_i was varied under reproducing each measured distribution of three kinds within the statistical uncertainty. The uncertainties in the acceptance were found to be 0.1–0.2 %, 0.2–0.4 %, and 0.6–0.7 % for the $M_{\pi d}$, $M_{\eta d}$, and $\cos\theta_d$ distributions, respectively. The uncertainty caused by the limited FOREST acceptance was 0.4–1.0 %. The uncertainty in the deuteron detection efficiency was 2.7–4.2 % due to the uncertainty in the density of the vacuum chamber surrounding the liquid deuterium target. The normalization uncertainties resulting from the number of target deuterons and from the number of incident photons were 1% and 2.3–2.7 %, respectively. The total systematic uncertainty $\delta\sigma_{\text{syst}}$ shown in Fig. 4 was obtained by combining all the uncertainties, $\delta\sigma_{\text{syst}}^i$s, described above in quadrature:

$$\delta\sigma_{\text{syst}}^2 = \sum \left(\sigma_{\text{syst}}^i\right)^2. \tag{8}$$

Our results for the total cross section are presented in Fig. 4. The MAMI data [44] are also shown for comparison. As can be seen, there is a slight systematic excess of our data, about 10% on average, which, however, is within the limits of the systematic error. Comparison with the theoretical calculations reveals fairly good reproducibility of the model in Ref. [28]. It is worth noting that at lower energies the impulse approximation with plane waves (red dashed curve) significantly underestimates the observed cross section. Its dependence on the total c.m. energy W is mainly determined by the reaction phase space $\mathcal{P}$, which for our reaction with three particles in the final state may be presented in the form

$$\mathcal{P} \sim \frac{1}{W E_\gamma} \int_{m_\eta + M_d}^{W - m_\pi} q_\pi(M_{\eta d})\, p_\eta(M_{\eta d})\, dM_{\eta d}, \tag{9}$$

where

$$\begin{aligned} q_\pi &= \frac{1}{2W} \lambda^{1/2}(W, M_{\eta d}, m_\pi) \text{ and} \\ p_\eta &= \frac{1}{2M_{\eta d}} \lambda^{1/2}(M_{\eta d}, m_\eta, M_d) \end{aligned} \tag{10}$$

are the pion momentum in the overall c.m. frame and the η momentum in the ηd c.m. frame, respectively.

The interaction between the η meson and the deuteron, due to its attractive character, leads to a visible increase of the plane-wave cross section. This effect is very typical for the processes in which interaction between the final particles is predominantly attractive. Within the time-independent quantum scattering theory, this is explained by the fact that the reaction rate is determined by the square of the matrix element sandwiched between the initial and final state vectors, namely, $|\gamma d\rangle$ and $|\pi^0 \eta d\rangle$ in our case, respectively. The latter, in turn, is proportional to the probability of finding the final particles in the region in which the initial interaction, leading to particle production, acts. Since attraction obviously tends to keep the final particles in this region, its presence leads to a

general increase of the reaction yield. The attractive character of the ηd interaction in the S wave is especially important at low energies, i.e., where the small values of p_η account for a significant fraction of the reaction phase space in Eq. (9). In our case, this results in strong increase of the plane-wave cross section at $E_\gamma < 0.9$ GeV.

As the energy increases, the FSI effect changes sign at about 1.05 GeV and at $E_\gamma = 1.15$ GeV results in a reduction of about 20% of the total cross section. This effect is expected to originate from the absorption of η mesons caused by their conversion into pions via $\eta N \to \pi N$. The η absorption due to inelastic resonance mechanisms is well known to be especially significant in inclusive processes on heavier nuclei [72], where it leads to the so-called surface production. In addition to the already mentioned pion absorption, the η absorption results in an additional decrease of the reaction yield over the entire energy range under consideration. Since the relative fraction of low ηd energies, at which the ηd attraction is significant, decreases with increasing photon energy, the role of absorption becomes especially noticeable at higher energies. As is seen from Fig. 4 this interplay between the enhancement due to ηd attraction and the absorption effects shifts the total cross section towards the threshold region.

In general, as one can conclude from Fig. 4, inclusion of the ηd interaction makes it possible to reproduce the experimental cross section in the energy range up to $E_\gamma < 1$ GeV. Above this region, some deviation between the theoretical calculation and the data is observed. In addition to the fact that the model of Ref. [28] may somewhat overestimate the role of absorption effects mentioned above, another possible reason for this discrepancy is that this model describes the elementary cross section $\gamma N \to \pi^0 \eta N$ only at the laboratory photon energies below 1.4 GeV. At higher energies, the resonances that are not included in the model must come into play, so that the calculation may visibly underestimate the data. When turning to a nucleus, this energy region is effectively incorporated into the calculation due to the Fermi motion, thus leading to some discrepancy which we just observe at higher energies.

The conclusions above apply also to the calculations presented in Ref. [71] (black curves in Fig. 4). Here the black solid curve shows the full calculation in which the FSI effects are taken into account in a unified microscopic approach, including pion rescattering on the spectator nucleon ($\gamma N_1 \to \pi^\pm \pi^0 N_1$ followed by $\pi^\pm N_2 \to \eta N_2$ and $N_1 N_2 \to d$), as well as absorption of an additionally produced pion on the spectator nucleon ($\gamma N_1 \to \pi^\pm \pi^0 \eta N_1$ followed by $\pi^\pm N_2 \to N_2$ and $N_1 N_2 \to d$). In this case, the full model is also in general agreement with the data in the region below 1 GeV. However, as the energy increases, the description is getting worse, as in the previous case.

C. Differential cross sections

To obtain more information about the important mechanisms of the $\gamma d \to \pi^0 \eta d$ reaction, we have also measured the invariant-mass and angular distributions: $d\sigma/dM_{\pi\eta}$, $d\sigma/dM_{\pi d}$, $d\sigma/dM_{\eta d}$, and $d\sigma/d\Omega_d$ in the energy bins $E_\gamma = 0.85$–0.94, 0.95–1.01, and 1.01–1.15 GeV. The differential
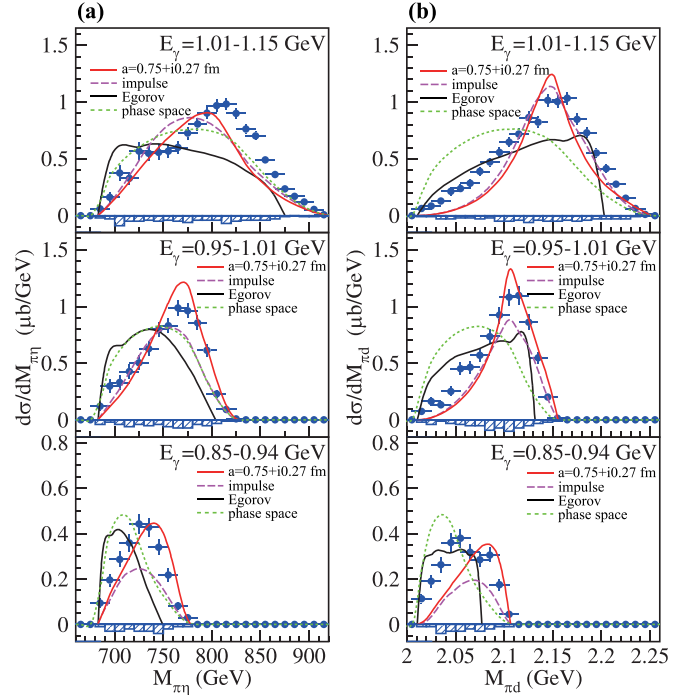

FIG. 5. Differential cross sections (a) $d\sigma/dM_{\pi\eta}$ and (b) $d\sigma/dM_{\pi d}$ for $E_\gamma = 0.85$–0.94 GeV (bottom), 0.95–1.01 GeV (center), and 1.01–1.15 GeV (top). The lower hatched histograms show the corresponding systematic errors. The green dotted curves represent the pure phase space. The magenta dashed and red solid curves show the impulse-approximation calculations, and the full calculations with the set of the ηN parameters corresponding to $a_{\eta N} = 0.75 + i\,0.27$ fm by Egorov and Fix [28]. The black solid curves show the full calculations by Egorov [71] at $E_\gamma = 0.90$, 0.98, and 1.08 GeV in the bottom, center, and top panels, respectively. The phase space is normalized so that the corresponding total cross section matches the measured one.

cross section $d\sigma/dV_i$ is given by

$$\frac{d\sigma}{dV_i}(E_\gamma, V_i)$$

$$= \frac{\mathcal{N}_{\pi\eta d}(E_\gamma, V_i)}{\mathcal{N}'_\gamma \mathcal{N}_\tau \mathcal{A}(E_\gamma, V_i)\mathcal{B}(\pi^0 \to \gamma\gamma)\mathcal{B}(\eta \to \gamma\gamma)\Delta V_i} \tag{11}$$

with V_i being one of the quantities $M_{\pi\eta}$, $M_{\pi d}$, $M_{\eta d}$, or $\cos\theta_d$. Due to axial symmetry with respect to the incident beam direction the simple relation $d\sigma/d\Omega_d = d\sigma/d\cos\theta_d/2\pi$ holds.

The results are presented in Figs. 5 and 6. The experimental data are depicted by blue circles with statistical errors, whereas the systematic uncertainties are shown by the hatched histograms. Here, the total systematic uncertainties for the differential cross sections were obtained by combining all the uncertainties discussed in Sec. IV B except those for the overall normalization (the uncertainties in the number of the target deuterons and in the number of the incident photons). The data are compared with the pure phase space plotted by the green dotted curves. The magenta dashed, red solid, and orange dotted curves show the calculations based on
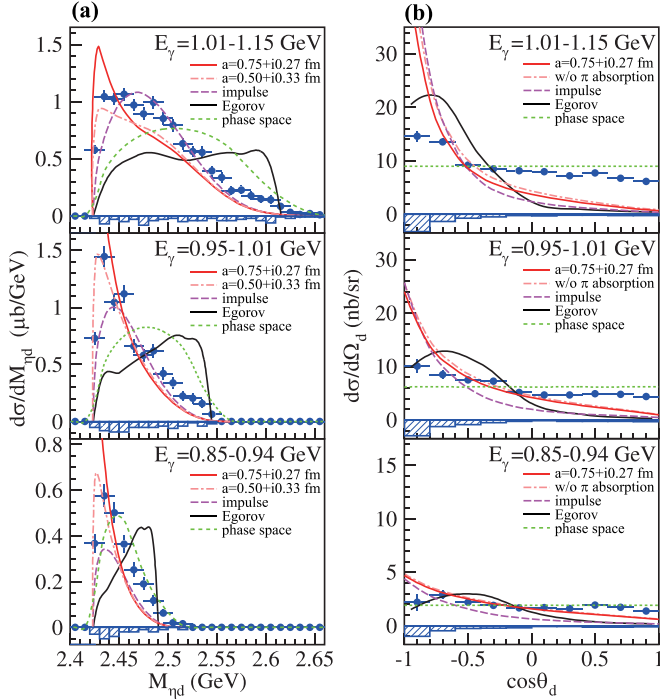
FIG. 6. Differential cross sections (a) $d\sigma/dM_{\eta d}$ and (b) $d\sigma/d\Omega_d$. The meaning of the curves is the same as in Fig. 5, except for the orange dot-dashed curves which are obtained with the sets of the ηN parameters, corresponding to $a_{\eta N} = 0.50 + i\,0.33$ fm in $d\sigma/dM_{\eta d}$, and $a_{\eta N} = 0.75 + i\,0.27$ fm in $d\sigma/d\Omega_d$. The pion absorption effect is not included in the latter case, and that is different from the red solid curves.

the impulse approximation, and the full calculation with FSI from Ref. [28] with different sets of the ηN interaction parameters (corresponding to $a_{\eta N} = 0.75 + i\,0.27$ fm [73] and $a_{\eta N} = 0.50 + i\,0.33$ fm [74]). The black solid curves are the full calculations by Egorov [71].

The mass distribution $d\sigma/dM_{\pi\eta}$ shown in Fig. 5(a) demonstrates a fairly smooth dependence, which differs only little in shape from the corresponding plane-wave distribution. This, in particular, is an obvious consequence of the absence of any resonant $\pi\eta$ interaction in the region under study. At low energies (lower panels), the overall increase of the reaction yield due to ηd attraction results in a noticeable increase of the plane-wave cross section, without a significant change of its shape. On the whole, as we see, the situation is similar to that noted above for the total cross section. Namely, the impulse approximation visibly underestimates the data, while inclusion of interaction in the final state makes it possible to substantially improve the agreement. The calculations by Egorov underestimate the data in the high-mass region. As discussed later, some features originating from the elementary amplitudes do not appear in mass distributions of his calculations in contrast to the calculations by Egorov and Fix and to the experimental data. There exists some problem in the treatment of the Born terms in his calculation.

A similar picture is observed in the case of the $d\sigma/dM_{\pi d}$ distribution shown in Fig. 5(b). Here the shape of the plane-wave cross section generally agrees with the data. A

noticeable difference is seen only in the bin $E_\gamma = 0.85$–0.94 GeV, where the theoretical cross section is slightly shifted to the higher mass. At higher energies, the distribution $d\sigma/dM_{\pi d}$ exhibits a clearly visible maximum at $M_{\pi d} \approx M_N + M_\Delta$, which apparently corresponds to the formation of $\Delta(1232)$. As one can see from the figure, although the position of the maximum is predicted fairly well by the theoretical calculations, there is a visible underestimation of the experimental cross section at the edges of the peak, especially in the lower part of the spectrum. The reason for this discrepancy is not very clear. It is quite possible that the approximation used in Ref. [28], in which the $\pi^0 d$ interaction is reduced to absorption and is described by a trivial attenuation factor, turns out to be too rough, and more refined effects have to be taken into account. In particular, it is well known that the three-body πNN calculations predict an $N\Delta$ resonance with $I(J^\pi) = 0(2^+)$, having a mass approximately equal to $M_N + M_\Delta$ (see, e.g., Refs. [75,76]). This resonance might influence the reaction dynamics, and its inclusion might improve the agreement. We will turn to this issue again in Sec. V.

Perhaps the most interesting is the distribution $d\sigma/dM_{\eta d}$ shown in Fig. 6(a). Here, the *S*-wave attraction between the η-meson and the deuteron leads to a rapid rise of the cross section in the region of low relative momenta in the ηd system. However, although the data generally demonstrate this trend, the sharpness of the maximum in the experimental cross section at $M_{\eta d} \approx M_\eta + M_d$ turns out to be less pronounced. This is especially evident in the high energy region $E_\gamma = 1.01$–1.15 GeV. Here, the agreement with the plane-wave cross section is even somewhat better than when the interaction is taken into account.

As for the theoretical predictions of Ref. [71] (solid black curves in Figs. 5 and 6), they strongly contradict our data. What is important, even the most characteristic features of the spectra, such as the Δ maximum in the $d\sigma/dM_{\pi d}$ distribution and the rapid rise of $d\sigma/dM_{\eta d}$ at $M_{\eta d} \to M_\eta + M_d$, are not reproduced by this model. The reasons for such a principle disagreement are obviously difficult to understand without a detailed analysis of the individual mechanisms included in this calculation.

It is also worthwhile to note a significant difference between the theoretical calculations and our data for the deuteron angular distribution $d\sigma/d\Omega_d$ in Fig. 6(b). The model in Ref. [28] predicts a rather sharp maximum at backward angles. Such a strong angular dependence is due to the coherent nature of the reaction mechanism. As a consequence, the cross section is basically governed by the square of the deuteron scalar form factor, which falls rapidly with increasing momentum transfer. This, in turn, leads to a rapid decrease of the cross section, so that its major fraction is located in a rather narrow region of the very backward deuteron angles θ_d. With increasing photon energy, the range of the available momentum transfer also increases, leading to stronger sharpening of the cross section at the maximum.

As can be seen from the figure, this simple picture is generally not confirmed by the measurements. In contrast to the theoretical calculation, the observed cross section demonstrates a fairly smooth dependence on $\cos\theta_d$, so that in the region of the forward deuteron angles, the difference reaches
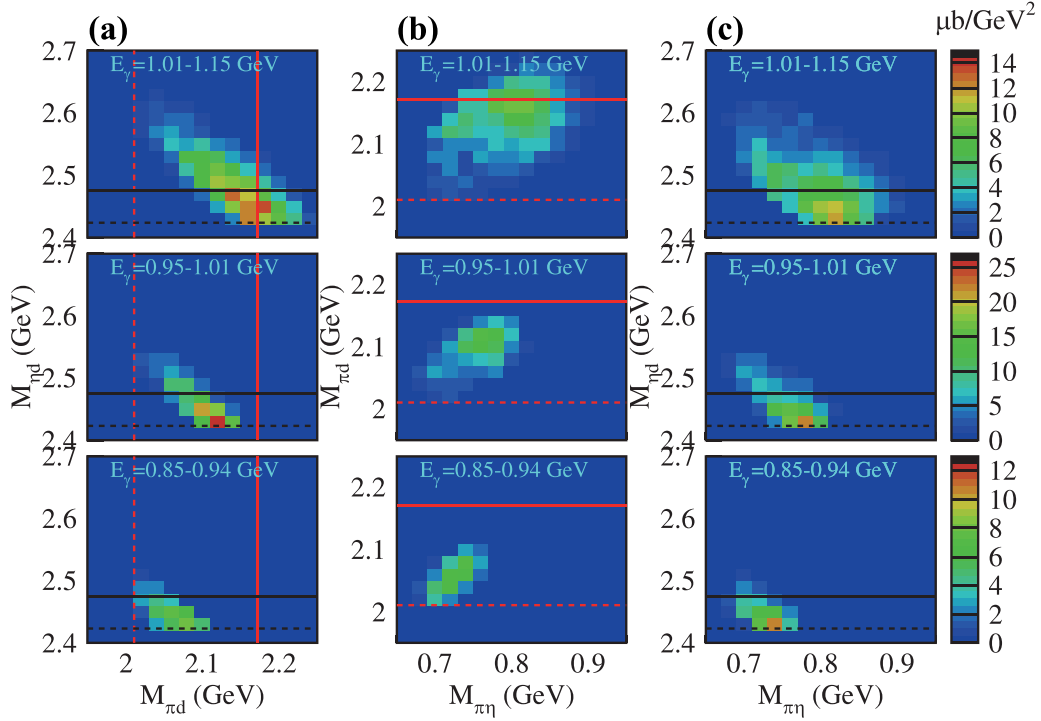
FIG. 7. Double-differential cross sections (a) $d^2\sigma/dM_{\eta d}/dM_{\pi d}$, (b) $d^2\sigma/dM_{\pi d}/dM_{\pi \eta}$, and (c) $d^2\sigma/dM_{\eta d}/dM_{\pi \eta}$ for $E_\gamma = 0.85$–0.94 GeV (bottom), 0.95–1.01 GeV (center), and 1.01–1.15 GeV (top). The red solid (dashed) lines represent $M_{\pi d} = M_N + M_\Delta$ ($M_{\pi^0} + M_d$), and the black solid (dashed) indicate $M_{\eta d} = M_N + M_{N^*}$ ($M_\eta + M_d$) where N^* stands for $N(1535)1/2^-$.

one order of magnitude. Furthermore, there is no sign in the data for the sharp maximum for the backward going deuterons, as predicted by the model. The calculations by Egorov do not show a peak at $\cos\theta_d = -1$. However, they also strongly underestimate the data at forward angles.

This result is somewhat unexpected, since, as mentioned above, the main factor determining $d\sigma/d\Omega_d$ is the deuteron form factor. Other components such as elementary amplitude are of secondary importance here. In this regard, this angular distribution is expected to have weak model dependence, so that the use of a sophisticated deuteron wave function should be sufficient for a realistic description of this observable. This notion is, however, in qualitative disagreement with the data. It is especially surprising that the difference turns out to be

so large. It looks as if there is some additional very important mechanism that allows the large transferred momentum to be shared between the nucleons, and thus increases the cross section at forward deuteron angles. To understand the situation better, further research in this area is needed.

D. Double-differential cross sections

To investigate correlation between two of the invariant masses $M_{\pi\eta}$, $M_{\eta d}$, and $M_{\pi d}$, we also deduced the double-differential cross sections $d^2\sigma/dM_{\eta d}/dM_{\pi d}$, $d^2\sigma/dM_{\pi d}/dM_{\pi \eta}$, and $d^2\sigma/dM_{\eta d}/dM_{\pi \eta}$. A double-differential cross section is given by

$$\frac{d^2\sigma}{dV_i\,dV_j}(E_\gamma, V_i, V_j) = \frac{\mathcal{N}_{\pi\eta d}(E_\gamma, V_i, V_j)}{\mathcal{N}'_\gamma\,\mathcal{N}_\tau\,\mathcal{A}(E_\gamma, V_i, V_j)\,\mathcal{B}(\pi^0 \to \gamma\gamma)\,\mathcal{B}(\eta \to \gamma\gamma)\,\Delta V_i\,\Delta V_j},$$

(12)

where V_i and V_j stand for two independent invariant masses from $M_{\pi\eta}$, $M_{\eta d}$, and $M_{\pi d}$. Figures 7(a), 7(b), and 7(c) show the obtained double-differential cross sections $d^2\sigma/dM_{\eta d}/dM_{\pi d}$, $d^2\sigma/dM_{\pi d}/dM_{\pi \eta}$, and $d^2\sigma/dM_{\eta d}/dM_{\pi \eta}$, respectively, together with the red solid (dashed) lines representing $M_{\pi d} = M_N + M_\Delta$ ($M_{\pi^0} + M_d$), and the black solid (dashed) indicating $M_{\eta d} = M_N + M_{N^*}$ ($M_\eta + M_d$), where N^* stands for $N(1535)1/2^-$.

The correlation between $M_{\eta d}$ and $M_{\pi d}$ at $E_\gamma = 1.01$–1.15 GeV in Fig. 7(a) shows an enhancement near the point $(M_{\pi d}, M_{\eta d}) = (M_N + M_\Delta, M_\eta + M_d)$. Whether or not the enhancement at $E_\gamma = 0.85$–0.94 and 0.95–1.01 GeV actually shows up is unclear, since the phase space does not cover $M_{\pi d} = M_N + M_\Delta$. An enhancement near the ηd threshold is seen in Fig. 7(c) at all the incident energies in the $(M_{\eta d}, M_{\pi \eta})$ plot. Additionally, an enhancement at $M_{\pi d} = M_N + M_\Delta$ is
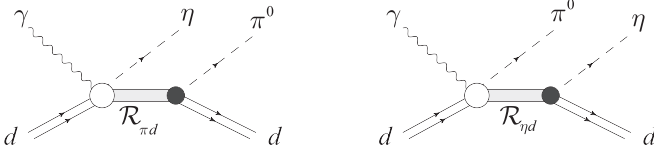
FIG. 8. Schematic representation of the $\gamma d \to \pi^0 \eta d$ amplitude (13) used in our phenomenological analysis.

observed at $E_\gamma = 1.01$–1.15 GeV in the $(M_{\pi d}, M_{\pi \eta})$ plot as shown in Fig. 7(b). Because of the limited phase space, it is difficult to distinguish the two conditions $M_{\pi d} \approx M_N + N_\Delta$ and $M_{\eta d} \approx M_\eta + M_d$. However, the lower edge of the peak near the ηd threshold does not visibly change, regardless of incident energies, and the peak becomes wider at higher incident energies. The resonance like structure in the $\pi^0 d$ channel, which is clearly observed near $M_{\pi d} = M_N + M_\Delta$ at the highest incident energies, is the main source of broadening of the maximum in the ηd spectrum, resulting from the strong ηd attraction.

V. PHENOMENOLOGICAL ANALYSIS

As discussed in the previous section, the microscopic models of Refs. [28,71] are unable to explain some important properties of the $\gamma d \to \pi^0 \eta d$ reaction observed in the experiment. In this regard, for further analysis, we use a purely phenomenological model, in which the amplitude consists of two terms,

$$T = T_{\pi(\eta d)} + T_{\eta(\pi d)}, \tag{13}$$

schematically illustrated in Fig. 8. Our method follows the same lines as in Ref. [48], where similar questions were addressed for the $NN(1535)1/2^-$ interaction.

For the intermediate quasi-two-body states $\mathcal{R}_{\eta d}$ and $\mathcal{R}_{\pi d}$ we adopt the pole approximation. In particular, in $\pi^0 d$ we took into account the previously mentioned pole, predicted by Faddeev calculations of the πNN system in the $I(J^\pi) = 1(2^+)$ state [75,76], sometimes treated in the literature as the $N\Delta$ dibaryon resonance $\mathcal{D}_{12}(2150)$ [75]. This configuration corresponds to the $L_J = P_2$ state in the πd system. The pole position predicted by the theoretical calculations is approximately at $2.10 + i0.14$ GeV. The corresponding πd scattering phase shift δ_{P_2} demonstrates purely resonant behavior, which is accompanied by a rapid decrease of the inelasticity parameter [76]. The other phase shifts are rather small in the energy region considered and can be neglected. Therefore, for $\mathcal{R}_{\pi d}$, we use the pure Breit-Wigner ansatz in the $1(2^+)$ partial wave, in which the mass M and the width Γ are treated as adjustable parameters.

The ηd pole in the $I(J^\pi) = 0(1^-)$ configuration is located near the ηd threshold energy. The results of various analyses [73,77,78] indicate that this pole is on the unphysical sheet so that it generates a virtual ηd state. For $\mathcal{R}_{\eta d}$, the Flatté parametrization [79,80] was adopted in Ref. [48], allowing us to take into account the closeness of the virtual ηd level to the threshold energy. To deduce the ηd scattering parameters $a_{\eta d}$ and $r_{\eta d}$, we replaced the Flatté ansatz by the low-energy
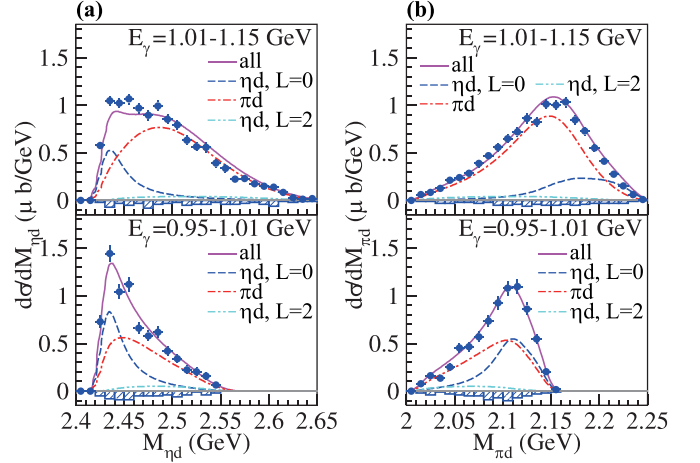

FIG. 9. Differential cross sections (a) $d\sigma/dM_{\eta d}$ and (b) $d\sigma/dM_{\pi d}$ together with the fitted functions (magenta solid curves) at $E_\gamma = 0.95$–1.01 GeV (bottom) and 1.01–1.15 GeV (top). The blue dashed and cyan double-dotted curves show the S- and D-wave decay contributions of $\mathcal{R}_{\eta d}$, respectively. The red dot-dashed curves represent the contribution from the second term in Eq. (16).

formula

$$\mathcal{R}_{\eta d} \sim \left(\frac{1}{a_{\eta d}} + \frac{1}{2} r_{\eta d} \, p_\eta^2 - i p_\eta \right)^{-1}, \tag{14}$$

where p_η is as previously the η momentum in the ηd c.m. frame. For completeness, in addition to the dominant $L = 0$ decay we also allow the $L = 2$ transition of $\mathcal{R}_{\eta d}$ to the final ηd state.

The simultaneous fit was performed to the $d\sigma/dM_{\eta d}$ and $d\sigma/dM_{\pi d}$ data at $E_\gamma = 1.01$–1.15 GeV and $E_\gamma = 0.95$–1.01 GeV. The fitted functions are built according to (see also Eqs. (1)–(4) in Ref. [48])

$$\frac{d\sigma}{dM_{\eta d}} = \alpha_0 \int A(M_{\eta d}, M_{\pi d}) V_{\rm PS}(M_{\eta d}, M_{\pi d}) \, dM_{\pi d}, \tag{15}$$

where $V_{\rm PS}(M_{\eta d}, M_{\pi d})$ is the reaction phase space and $A(M_{\eta d}, M_{\pi d})$ is given by

$$A(M_{\eta d}, M_{\pi d})$$
$$= \left(1 + \alpha_2 \, p_\eta^4 \right) |\mathcal{R}_{\eta d}(M_{\eta d})|^2 + \alpha_1 \, |\mathcal{R}_{\pi d}(M_{\pi d})|^2. \tag{16}$$

Here, the experimental mass resolutions are convoluted in the evaluation of Eq. (15). Similarly to Ref. [48], we neglect in Eq. (16) the interference of the $\gamma d \to \pi^0 \mathcal{R}_{\eta d} \to \pi^0 \eta d$ and $\gamma d \to \eta \mathcal{R}_{\pi d} \to \pi^0 \eta d$ transitions. This approximation may not be crucial since the angular momentum of η emission differs between the corresponding mechanisms [48]. For the $d\sigma/dM_{\pi d}$ distribution, a similar expression was used, where the integration is carried out, of course, over $M_{\eta d}$.

Our solution is presented in Fig. 9, where the contributions determined by the two terms in Eq. (16) are separately shown. The resulting χ^2 value is 131.3 for 76 data points. The $\pi^0 d$ parameters coming out of the fit are $M = 2.158^{+0.003}_{-0.003}$ GeV and $\Gamma = 0.116^{+0.004}_{-0.007}$ GeV, respectively. They are consistent

with the results of the mass fit with Flatté parametrization in Ref. [48]. Furthermore, they are quite close to $M = 2.147$, $\Gamma = 0.12$ and $M = 2.091$, $\Gamma = 0.16$ obtained for the $N\Delta$ $\mathcal{D}_{12}$ resonance within the three-body calculations in Refs. [75] and [76], respectively.

Adjusting the model parameters to the $d\sigma/dM_{\eta d}$ and $d\sigma/dM_{\pi d}$ data at $E_\gamma = 0.95$–1.01 and 1.01–1.15 GeV gives $a_{\eta d} = \pm(0.7^{+0.8}_{-0.6}) + i(0.0^{+1.5}_{-0.0})$ fm and $r_{\eta d} = \mp(4.3^{+8.6}_{-2.9}) - i(6.7^{+6.0}_{-8.4})$ fm. Here, the double sign in $r_{\eta d}$ corresponds to that in $a_{\eta d}$. It cannot be uniquely determined from the fit. However, for qualitative agreement with the theoretical results [73,77,78] which support only a virtual ηd level, a plus sign of $a_{\eta d}$ must be taken. The $d\sigma/dM_{\eta d}$ and $d\sigma/dM_{\pi d}$ obtained in this work are rather insensitive to $r_{\eta d}$ due to the limited phase space at $E_\gamma < 1.15$ GeV, making the statistical error of $r_{\eta d}$ quite large. These large uncertainties also make it difficult to determine $a_{\eta d}$ more or less precisely. The value of $a_{\eta d}$ thus obtained is in reasonable agreement with the three-body results. In particular, it is quite close to $a_{\eta d} = 1.23 + i\,1.11$ fm obtained in Ref. [28] with a set of ηN parameters ($a_{\eta N} = 0.50 + i\,0.33$ fm) adjusted to the ηN scattering amplitude from Ref. [74].

VI. SUMMARY

The $\gamma d \to \pi^0\eta d$ reaction has been experimentally studied at $E_\gamma < 1.15$ GeV. We have measured the total cross section σ as a function of E_γ, which demonstrates a rapid rise in the region from $E_\gamma = 0.8$ up to 1 GeV. The existing theoretical calculations incorporating microscopic treatment of final-state interaction reproduce $\sigma(E_\gamma)$ rather well. As our analysis shows, taking into account the interaction effect noticeably influences the result and is of decisive importance for the observed fairly good agreement between theoretical calculation and experimental data.

We have also measured the differential cross sections $d\sigma/dM_{\pi\eta}$, $d\sigma/dM_{\pi d}$, $d\sigma/dM_{\eta d}$, and $d\sigma/d\Omega_d$ for the first time. The ηd interaction is clearly seen in the ηd-invariant mass spectrum $d\sigma/dM_{\eta d}$. The corresponding enhancement due to the large scattering length $a_{\eta d}$ is qualitatively reproduced by the theoretical calculation, although it predicts a too sharp maximum at the ηd threshold. The difference between the calculation and the experimental results for $d\sigma/dM_{\eta d}$ becomes especially noticeable with increasing energy.

The ηd scattering parameters obtained from the phenomenological analysis of $d\sigma/dM_{\eta d}$ and $d\sigma/dM_{\pi d}$ are $a_{\eta d} = \pm(0.7^{+0.8}_{-0.6}) + i(0.00^{+1.5}_{-0.0})$ fm and $r_{\eta d} = \mp(4.3^{+8.6}_{-2.9}) - i(6.7^{+6.0}_{-8.4})$ fm, where the double sign in $r_{\eta d}$ corresponds to

that in $a_{\eta d}$. Because of the uncertain sign of Re$[a_{\eta d}]$, it is not clear whether a bound or a virtual ηd state is generated. The existing microscopic theories generally support the idea that the strength of the ηd interaction is not sufficient to bind this system, so that the observed increase should be associated with a virtual ηd level.

The model predictions for the angular distribution $d\sigma/d\Omega_d$ exhibit a pronounced maximum at the very backward deuteron angles. As discussed in Sec. IV C such dependence is mainly governed by the strong dependence of the deuteron form factor on the momentum transfer. At the same time, the data show no sign for any sharp peaking for backward-going deuterons. As a result, in the forward deuteron hemisphere the data are underestimated by almost a factor of ten.

The sharp angular dependence, predicted by the theoretical calculations, might be softened by different second order processes, in which the spectator nucleon is also involved and thus the transferred momentum is shared between the both nucleons. However, direct calculations show that the effect of such mechanisms is limited and does not allow one to explain the observed difference. Since the discrepancies in the deuteron angular distribution are rather serious, they give reason to doubt the validity of our general notion about the main mechanisms of the $\gamma d \to \pi^0\eta d$ reaction (impulse approximation plus interaction in the final state). Therefore, further research in this area is highly desirable.

ACKNOWLEDGMENTS

[1] V. Bernard and U.-G. Meißner, Nucl. Phys. A **489**, 647 (1988).

[2] G. E. Brown and M. Rho, Phys. Rev. Lett. **66**, 2720 (1991).

[3] T. Hatsuda and S. H. Lee, Phys. Rev. C **46**, R34 (1992).

[4] S. D. Bass and A. W. Thomas, Phys. Lett. B **634**, 368 (2006).

[5] S. Hirenzaki and H. Nagahiro, Acta Phys. Pol. B **45**, 619 (2014).

[6] S. D. Bass and P. Moskal, Rev. Mod. Phys. **91**, 015003 (2019).

[7] C. DeTar and T. Kunihiro, Phys. Rev. D **39**, 2805 (1989).

[8] T. Hatsuda and M. Prakash, Phys. Lett. B **224**, 11 (1989).

[9] D. Jido, H. Nagahiro, and S. Hirenzaki, Phys. Rev. C **66**, 045202 (2002).

[10] H. Nagahiro, D. Jido, and S. Hirenzaki, Phys. Rev. C **68**, 035205 (2003).

[11] H. Nagahiro, D. Jido, and S. Hirenzaki, Nucl. Phys. A **761**, 92 (2005).

[12] D. Jido, E. E. Kolomeitsev, H. Nagahiro, and S. Hirenzaki, Nucl. Phys. A **811**, 158 (2008).
[13] T. Yorita *et al.*, Phys. Lett. B **476**, 226 (2000).
[14] T. Kinoshita *et al.*, Phys. Lett. B **639**, 429 (2006).
[15] B. Mayer *et al.*, Phys. Rev. C **53**, 2068 (1996).
[16] J. Smyrski *et al.*, Phys. Lett. B **649**, 258 (2007).
[17] T. Mersmann *et al.*, Phys. Rev. Lett. **98**, 242301 (2007).
[18] M. Pfeiffer *et al.*, Phys. Rev. Lett. **92**, 252001 (2004).
[19] M. Pfeiffer *et al.*, Phys. Rev. Lett. **94**, 049102 (2005).
[20] F. Pheron *et al.*, Phys. Lett. B **709**, 21 (2012).
[21] B. Krusche and C. Wilkin, Prog. Part. Nucl. Phys. **80**, 43 (2014).
[22] Y. Maghrbi *et al.* (Crystal Ball at MAMI, TAPS, and A2 Collaborations), Eur. Phys. J. A **49**, 38 (2013).
[23] H. Calén *et al.*, Phys. Rev. Lett. **79**, 2642 (1997).
[24] H. Calén *et al.*, Phys. Rev. Lett. **80**, 2069 (1998).
[25] F. Hibou *et al.*, Eur. Phys. J. A **7**, 537 (2000).
[26] R. Bilger *et al.*, Phys. Rev. C **69**, 014003 (2004).
[27] U. Tengblad, G. Fäldt, and C. Wilkin, Eur. Phys. J. A **25**, 267 (2005).
[28] M. Egorov and A. Fix, Phys. Rev. C **88**, 054611 (2013).
[29] N. N. Achasov and G. N. Shestakov, JETP Lett. **92**, 1 (2010).
[30] M. Döring, E. Oset, and D. Strottman, Phys. Rev. C **73**, 045209 (2006).
[31] A. Fix, V. L. Kashevarov, A. Lee, and M. Ostrick, Phys. Rev. C **82**, 035207 (2010).
[32] T. Nakabayashi *et al.*, Phys. Rev. C **74**, 035202 (2006).
[33] J. Ajaka *et al.*, Phys. Rev. Lett. **100**, 052003 (2008).
[34] I. Horn *et al.* (CB-ELSA Collaboration), Eur. Phys. J. A **38**, 173 (2008).
[35] I. Horn *et al.* (CB-ELSA Collaboration), Phys. Rev. Lett. **101**, 202002 (2008).
[36] E. Gutz *et al.* (CB-ELSA/TAPS Collaboration), Eur. Phys. J. A **35**, 291 (2008).
[37] I. Jaeglé (CB-ELSA/TAPS Collaboration), Chin. Phys. C **33**, 1340 (2009).
[38] E. Gutz *et al.* (CB-ELSA/TAPS Collaboration), Phys. Lett. B **687**, 11 (2010).
[39] E. Gutz *et al.* (CB-ELSA/TAPS Collaboration), Eur. Phys. J. A **50**, 74 (2014).
[40] V. Sokhoyan *et al.*, Phys. Rev. C **97**, 055212 (2018).
[41] V. L. Kashevarov *et al.* (Crystal Ball at MAMI, TAPS, and A2 Collaborations), Eur. Phys. J. A **42**, 141 (2009).
[42] V. L. Kashevarov *et al.* (Crystal Ball at MAMI, TAPS, and A2 Collaborations), Phys. Lett. B **693**, 551 (2010).
[43] J. R. M. Annand *et al.* (A2 Collaboration at MAMI), Phys. Rev. C **91**, 055208 (2015).
[44] A. Käser *et al.*, Phys. Lett. B **748**, 244 (2015).
[45] A. Käser *et al.* (A2 Collaboration), Eur. Phys. J. A **52**, 272 (2016).
[46] A. Käser *et al.*, Phys. Lett. B **786**, 305 (2018).
[47] B. Krusche, Eur. Phys. J.: Spec. Top. **198**, 199 (2011)
[48] T. Ishikawa *et al.*, Phys. Rev. C **104**, L052201 (2021).
[49] T. Ishikawa *et al.*, JPS Conf. Proc. **10**, 031001 (2016).
[50] T. Ishikawa *et al.*, Nucl. Instrum. Methods Phys. Res. Sect. A **622**, 1 (2010).
[51] F. Hinode *et al.*, in *Proceedings of 21st IEEE Particle Accelerator Conference (PAC)* (IEEE, Piscataway, NJ, 2005), pp. 2458–2460.
[52] H. Hama, AAPPS Bull. **30**, 41 (2020).
[53] Y. Obara *et al.*, Nucl. Instrum. Methods Phys. Res. Sect. A **922**, 108 (2019).
[54] T. Ishikawa *et al.*, Nucl. Instrum. Methods Phys. Res. Sect. A **811**, 124 (2016).
[55] Y. Matsumura *et al.*, Nucl. Instrum. Methods Phys. Res. Sect. A **902**, 103 (2018).
[56] H. Yamazaki *et al.*, ELPH Annual Report 2011–2013, Tohoku University, 2014 (unpublished), p. 126.
[57] R. Hashimoto *et al.*, Research Report of Laboratory of Nuclear Science No. 41, Tohoku University, 2008, p. 31 (unpublished).
[58] T. Ishikawa *et al.*, Nucl. Instrum. Methods Phys. Res. Sect. A **832**, 108 (2016).
[59] T. Ishikawa *et al.*, Nucl. Instrum. Methods Phys. Res. Sect. A **694**, 348 (2012).
[60] H. Fujimura *et al.*, Research Report of Laboratory of Nuclear Science No. 41, Tohoku University, 2008 (unpublished), p. 26.
[61] T. Ishikawa *et al.*, Phys. Lett. B **772**, 398 (2017).
[62] T. Ishikawa *et al.*, Phys. Lett. B **789**, 413 (2019).
[63] T. Ishikawa *et al.*, Phys. Rev. C **101**, 052201(R) (2020).
[64] T. Ishikawa *et al.*, ELPH Annual Report 2010, Tohoku University, 2011 (unpublished), p. 1.
[65] S. Agostinelli *et al.*, Nucl. Instrum. Methods Phys. Res. Sect. A **506**, 250 (2003).
[66] J. Allison *et al.*, IEEE Trans. Nucl. Sci. **53**, 270 (2006).
[67] Geant4 website, http://geant4.cern.ch/
[68] D. H. White, R. M. Schectman, and B. M. Chasan, Phys. Rev. **120**, 614 (1960).
[69] M. Bernheim *et al.*, Nucl. Phys. A **365**, 349 (1981).
[70] P. A. Zyla *et al.* (Particle Data Group), Prog. Theor. Exp. Phys. **2020**, 083C01 (2020).
[71] M. Egorov, Phys. Rev. C **101**, 065205 (2020).
[72] M. Röbig-Landau, J. Ahrens, G. Anton, R. Averbeck, R. Beck, M. Fuchs, A. R. Gabler, F. Härter, P. D. Harty, V. Hejny *et al.*, Phys. Lett. B **373**, 45 (1996).
[73] A. H. Green and S. Wycech, Phys. Rev. C **55**, R2167 (1997).
[74] C. Wilkin, Phys. Rev. C **47**, R938 (1993).
[75] A. Gal and H. Garcilazo, Nucl. Phys. A **928**, 73 (2014).
[76] O. Kolesnikov and A. Fix, J. Phys. G **48**, 085101 (2021).
[77] A. Fix and H. Arenhövel, Eur. Phys. J. A **9**, 119 (2000).
[78] N. Barnea, E. Friedman, and A. Gal, Phys. Lett. B **747**, 345 (2015).
[79] S. M. Flatté, Phys. Lett. B **63**, 224 (1976).
[80] Yu. S. Kalashnikova, and A. V. Nefedirev, Phys. Rev. D **80**, 074004 (2009).